

Chapter 2

Force-Fed Microchannels for High Flux Cooling Applications

Abstract In this chapter, the working principles of force-fed microchannel (micro-grooved) heat exchangers (FFMHX) in single-phase and two-phase heat transfer modes are defined and the associated benefits of using these systems are highlighted. The literature on FFMHX is reviewed, and important conclusions are summarized. The main benefits of optimally designed next generation force-fed heat transfer (FFHT) configurations are the short, parallel microchannel network system and equal flow distribution among the channels through careful manifold design. The collective benefits include substantially higher available heat/mass transfer surface area, precise flow distribution among the channels, creation of thin film cooling in microchannels such that the thin film component dominates the flow regime, and low to moderate pressure drops while achieving record-high heat/mass transfer coefficients. The information presented in this chapter includes experimental evaluation of the thermal performance of FFMHXs in two-phase heat transfer mode using refrigerant R-245fa. Two distinct heat transfer trends were observed. At high hydraulic diameter, high mass flux, and high heat flux, the heat transfer coefficients had a slowly increasing trend with increase in heat flux and outlet quality. At low hydraulic diameters, low mass flux, and low heat flux, the heat transfer coefficients experience a bell-shaped behavior with a sharp increase at low vapor qualities until they reach the maximum peak point. Most recent research has focused on increasing the vapor quality at the exit of the evaporator for energy efficiency and optimum system performance. It was demonstrated that the tested FFMHX heat sink configuration can cool a heat flux of $q''_{\text{base}} = 1.23 \text{ kW/cm}^2$ with a superheat of $\Delta T_{\text{sat}} = 56.2^\circ\text{C}$ and pressure drop of only $\Delta P = 60.3 \text{ kPa}$. The results clearly suggest that under optimum design conditions, FFMHXs have the proven potential to achieve substantially higher heat transfer coefficients with low

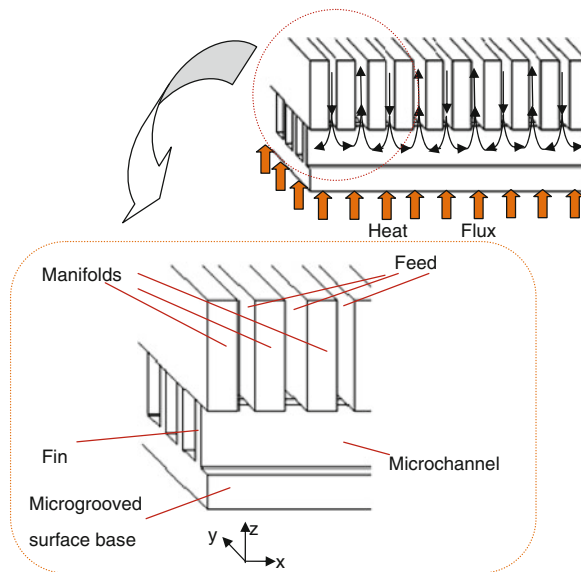
to moderate pressure drops, and substantially less working fluid in circulation, and thus substantial compaction (weight/volume reductions), improved energy efficiency, and reduced capital and operational cost. When compared to the state-of-the-art thermal management/conventional systems.

2.1 Introduction

High heat flux cooling is required in many applications such as power electronics, plasma-facing components, high heat-load optical components, laser diode arrays, X-ray medical devices, and power electronics in hybrid vehicles. In general, the exposed area that needs to be cooled for these systems is limited, and the amount of heat that needs to be removed is extremely high, thus requiring cooling of high heat fluxes. While high heat flux cooling is essential for creating an efficient cooling system, there are usually also other system requirements, such as low thermal resistance, surface temperature uniformity, low pumping power, compact design, suitability for large area cooling, and compatibility for use with dielectric fluids. Currently, most of the advanced electronic components already generate heat fluxes exceeding 100 W/cm^2 , while some future microprocessors and power-electronic components, such as high-power laser and electronic radar systems, have been projected to generate heat fluxes over $1,000 \text{ W/cm}^2$ (Mudawar 2001; Kandlikar 2005; Kandlikar and Bapat 2007). The increase in power density of the components has also created a need for advanced cooling technologies to achieve high heat dissipation rates in order to keep the electronic system at the desired working temperatures. At this point, traditional and well-known cooling methods will prove insufficient for such high heat fluxes.

The force-fed microchannel heat exchanger (FFMHX) concept (also known as the manifold microchannel heat sink) was first introduced by Harpole and Eninger (1991), and later studies reported that FFMHX can achieve heat transfer coefficients of 30–50 % (Kim and Chun 1998; Ryu and Choi 2003) higher than traditional microchannel heat sinks (TMHS) at the lowering pumping power. However, due to flow and their geometrically complex nature, FFMHXs in the past received less attention, and the flow and heat transfer associated with these heat sinks have not been studied in detail yet. This chapter provides an overview of the most recent progress in FFMHX and the basics of the heat transfer enhancement mechanism that makes this cooling technology unique. Differences from TMHS will also be highlighted.

Fig. 2.1 Schematic flow representation of a typical FFMHX (Cetegen 2010)



2.1.1 Working Principles

An FFMHX is basically a combination of a microgrooved surface and a system of manifolds. The flow schematic of a typical FFMHX is shown in Fig. 2.1. The flat side of the microgrooved surface is attached to the heat source, while the fins and microchannels on the other side are in contact with the working fluid. A series of parallel manifolds is located on the top of the microchannels and aligned perpendicularly to the fin structure. The manifolds do not contribute to heat transfer significantly, their primary role being to distribute the fluid and provide structural integrity to the FFMHX. Each gap between the two neighboring manifolds forms a feed channel, which is used to direct the fluid in (inlet feed channel) or out (outlet feed channel) of the microchannels. This gap can have similar or different dimensions for inlet and outlet feed channels, depending on the desired design configuration. From a design standpoint, compared with microchannels, the feed channels have much greater hydraulic diameters and lower flow velocities. The manifolds and the microgrooved surface are usually attached to each other by use of compressive force that seals the tip of the fins to the bottom of the manifolds.

The inlet feed channels in the manifold structure are designed to deliver the same flow resistance so that when they are connected to a common fluid source, flow uniformity can be easily achieved. The flow in the feed channels can be considered as flow between two parallel plates due to the usually high aspect ratio of the feed channels. After entering and flowing along the feed channel, the fluid encounters the microchannels and fins of the microgrooved surface. Here, the fluid is forced to enter the microchannel from the top, perpendicularly to the microchannel direction. This entrance creates a flow area reduction and in turn increases

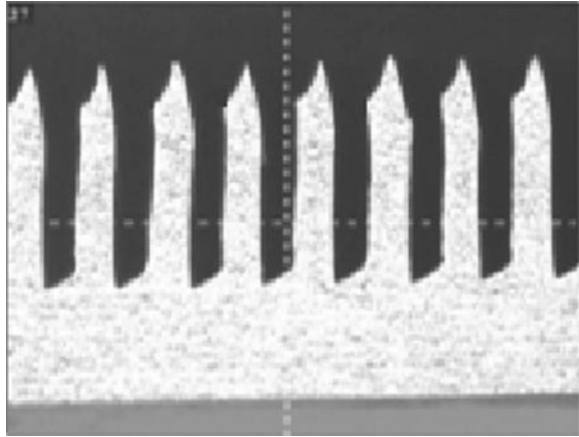
the flow velocity and decreases the static pressure at the entrance region of the microchannel. After entering the microchannel area, the flow starts to develop until it flows down to the bottom of the channel, eventually creating an impingement zone. After the stagnation point, the fluid splits into two streams, each stream turning 90° and flowing in the opposite directions in the microchannel. The fluid continues to flow a short distance in the microchannel and at this point the flow and heat transfer occur similarly to that in a typical TMHS. The distance of the straight microchannel is defined by the thickness of the manifolds. At the end of the straight microchannel, the fluid will make a second 90° turn, joining with the counterstream and leaving the area through the corresponding outlet feed channel. The exit from the microchannel to the outlet feed channel creates a pressure increase and velocity reduction due to an increase in flow area. This flow configuration is repetitive and results in the formation of arrays of short microchannels working in parallel.

The key geometrical arrangements and flow distributions that make FFMHX an effective heat transfer cooling system are as follows:

- The system pressure drop is decreased significantly due to the short flow length of the turning path in the microchannels. The system is, in fact, a network of short microchannels working in parallel, and therefore the total system pressure drop is the pressure drop of a single microchannel flow turn.
- FFMHX is suitable for cooling large areas and can be easily expandable in the x - y directions. By increasing the flow rate proportional to the base area expansion rate, the system pressure drop and effective heat transfer coefficient remain constant.
- FFMHX benefits from multiple inlet entrance effects. The area in the microchannel flow inlet region can yield very high heat transfer coefficients. This effect is the result of thermally developing flow in this region, which is associated with very thin boundary layers and low thermal resistance values. Multiple inlet regions enhance the overall heat transfer coefficient of the heat sink.
- Generally, electronic chips that need to be cooled are spaced closely together on the substrate, and there is limited space in the x - y direction for including additional equipment such as flow distributing manifolds. In this case, it could be more convenient to include additional parts in the z -direction, which makes FFMHX design favorable.

FFMHX design requires enhanced surfaces with alternating fins and channels, also known as microgrooved surfaces. These surfaces can be fabricated using several different methods, depending on the substrate material and geometric features. For example, the silicon microfabrication technique can create very fine surfaces with microchannels having hydraulic diameters on the order of microns. Micromachining is another process that can create microchannels using methods such as electron discharge machining (EDM) or laser ablation. These methods are the most suitable for metal substrates. Another fabrication method that is becoming more popular is micro deformation technology (MDT). This relatively new technology allows fabrication of enhanced surfaces with very high aspect

Fig. 2.2 Picture of a typical microgrooved surface profile fabricated with MDT (Thors and Zoubkov 2009)



ratio channels and fins from a wide range of metals. MDT was initially developed to produce enhanced heat transfer tubes and was later adopted for flat surfaces. The fabrication principle of MDT is based on a continuous process of skiving and bending material on the top of a metal substrate. The major advantage of MDT is that it can be cost effective when adapted for mass production (Thors and Zoubkov 2009).

A cross-section of a typical microgrooved surface fabricated using MDT is shown in Fig. 2.2. The fin geometry created by MDT is usually slightly different from the fin structure of a traditional microgrooved surface fabricated usually by the silicon microfabrication technique. Based on the cutting tool geometry used during fabrication, MDT microgrooved surfaces have an unconventionally sharp fin-tip and a slightly bent fin geometry.

2.1.2 Survey of State of the Art Research in the Field

The earliest study to introduce and investigate heat transfer and fluid flow in an FFMHX is by Harpole and Eninger (1991). They considered microchannels and manifolds etched from silicon and an optional diamond face sheet attached between the heat sink and heat source for heat spreading and enhancing the surface temperature uniformity. By neglecting the entrance effects and convective heat transfer by assuming a low Reynolds number flow and constant Nusselt number, they formulated the flow and heat transfer using a 2D model. Based on this model, they performed a parametrical analysis of the microchannel geometry and flow by varying one parameter and keeping the other parameters constant. They concluded that when water is used as a coolant, heat fluxes on the order of $1,000 \text{ W/cm}^2$ can be cooled effectively with pressure drop values on the order of 1 bar. They also noted that although the pressure losses at the inlet and outlet to the microchannels

were not considered in the model, they could be significant and needed to be included in a more detailed design.

Copeland (1995) analyzed flow and heat transfer in an FFMHX by assuming one-dimensional flow and building a simple model based on the hydrodynamically and thermally developing flow correlations in straight tubes. The heat sink material was assumed to be poorly conductive, and a uniform heat flux was applied to the base. Using the mathematical model, parametrical analyses were performed to investigate the variation of thermal resistance with flow and geometrical parameters. The analysis strategy was to investigate thermal resistance by varying two parameters at a time while keeping other parameters constant. The results showed that increasing the number of manifolds per unit length of heat sink can decrease thermal resistance, and for a given manifold number and pumping power there exists an optimum channel width and fin thickness. Copeland (1995) and Copeland et al. (1997) numerically analyzed the heat transfer and pressure drop in an FFMHX for 32 different cases with different geometries and inlet flow conditions. The computational domain was simplified by neglecting the conjugate heat transfer in the solid part of the microgrooved surface. Therefore, only the fluid flow was modeled, and constant heat flux or constant temperature boundary condition was applied to all heat transfer surfaces (microchannel base and fin surfaces). Their model also neglected the heat transfer from the tip of the fins and the pressure losses due to both flow contraction and expansion at the inlet and outlet to the microchannels.

Based on the numerical results, two different heat transfer characteristics were observed. The first heat transfer mode occurred at low channel velocities of 0.1 m/s. In these cases, the local heat transfer coefficients peaked at the inlet region and then gradually decreased to the end of the microchannel. The second mode of heat transfer was reported at high flow velocities of 1 m/s. Here, the local heat transfer coefficient was nonuniformly distributed along the channel walls, with the maximum close to the inlet region and two other local maxima at the channel bottom below the inlet and close to the outlet at the end of microchannel. Although not reported in their study, these different heat transfer characteristics are the result of flow impingement and secondary flow-induced vortices, which can create local maximum heat transfer coefficient regions. The study also compared the numerical results with 1D straight channel models, and it was found that such a simplified model failed to predict the pressure drop and thermal resistance values obtained by numerical simulations.

Kim and Chun (1998) experimentally investigated the thermal performance of FFMHXs for air cooling. Several experimental tests were performed for nine different copper microgrooved surfaces and two manifold systems with different geometrical dimensions. As a general trend for all cases, they found that thermal resistance is a strong function of flow rate and that thermal resistance decreases linearly with increasing pumping power on a log–log plot. Among the investigated geometrical parameters, microchannel width and manifold inlet and outlet feed channel widths were found to affect the thermal resistance the most. Interestingly, they also reported that for two heat sinks with identical microgrooved surfaces but

different manifold designs, increasing manifold number per unit heat sink length increased thermal resistance at the same pumping power. This result conflicts with the work of Copeland (1995), where it was shown that increasing the manifold number had a beneficial effect on decreasing thermal resistance. The geometrical design that delivered the lowest thermal resistance was compared with a traditional microchannel heat sink, and it was found that the FFMHX design would work with 35 % less thermal resistance at the same pumping power.

Ng and Poh (1999) analyzed thermal performance of FFMHXs numerically for 16 cases with different geometrical dimensions and flow conditions. The numerical model was validated by the experimental results of Copeland (1995). They also formulated a 1D analytical model based on straight channel pressure drop and heat transfer correlations. The numerical model was compared with the analytical model for thermal resistance at similar geometrical and flow parametric input conditions. The comparison showed that the 1D analytical model could predict the thermal resistance values at an acceptable range only at very low Reynolds numbers ($Re < 50$). At higher Reynolds numbers, the analytical model largely under-predicted (up to 400 %) the thermal resistance values. Overall, it was concluded that simple 1D analytical models based on straight channel flow cannot predict the thermal performance of an FFMHX accurately.

Ryu and Choi (2003) analyzed the heat transfer and flow in an FFMHX by numerically solving the 3D Navier Stokes equations. Using a finite volume approach, their numerical model considered both the convective heat transfer in the channel and the heat transfer through the fins and base material. The base material selected was silicon, and water was used as the working fluid. By keeping the pumping power and manifold number constant and varying other parameters, they optimized the geometry using a steepest-descent technique to minimize the thermal resistance. They compared their results with TMHS and reported that the thermal resistance could be reduced by more than half, while the temperature uniformity on the heated wall could be improved by tenfold.

Jankowski and Everhart (2007) explored experimentally the possibility of reducing the thermal resistance of power electronics used in hybrid vehicles by integrating two different cooling systems involving microchannels. The first approach consisted of integrating an FFMHX to cool chips directly on a silicon substrate. The second approach used a TMHS with microchannels created in an aluminum nitride substrate. The thermal resistance values for both systems were measured at pressure drops of 17 and 35 kPa. The results show that the thermal resistance values for both systems were comparable at 17 kPa, and for 35 kPa FFMHX thermal resistance was lower by only about 12 % compared with the THMS design. The authors attributed this low difference to the nonoptimized geometries of FFMHX and suggested that the heat transfer geometry needed to be optimized for future potential improvement.

Xia and Liu (2008) investigated experimentally the effect of two different surfactants on pressure drop in a single-channel manifold microchannel with the goal of increasing the system drag reduction. They used sodium dodecyl sulphate and alkyl polyglycoside aqueous solutions as working fluids. They found that the measured

drag reduction values were not significant for laminar flow regime, but that the pressure drop reduction was more effective in transition flow at high temperatures. The transition from laminar flow to transitional flow occurred at a critical Reynolds number of 800.

Haller et al. (2009) investigated experimentally and numerically the pressure loss and heat transfer in bending and branching microchannels such as L-bends and T-joints for rectangular channels with a 90° turning angle. This geometrical configuration is similar to a unit cell of an FFMHX without the second turning bend at the end of the microchannel. Using water, they tested silicon-based channel flow for Reynolds numbers ranging from 10 to 3,000. Based on both numerical and experimental results, they reported that flow turning can enhance the heat transfer when fluid was redirected in the 90° bend. This effect was the result of flow vortices induced by secondary flows created by centrifugal forces. They also reported that the creation of such vortices also increased the pressure drop of the system due to higher viscous dissipation losses. The heat transfer efficiency and pressure drop characteristics were found to be always conflicting, with higher heat transfer performance always requiring higher pumping power. They also unsuccessfully attempted to model the pressure loss of the laminar flow in microchannel bends with vortices. They conceded that the main challenge of building such a model is the different flow characteristics observed at different flow conditions and channel geometries. For example, the creation of no vortices, or one pair or two pairs of vortices was strongly dependent on Reynolds number, shape, and aspect ratios of the channel.

Cetegen et al. (2007, 2008) performed experimental tests to determine the boiling heat transfer performance of FFMHX for different microgrooved surfaces and working fluids. They were able to show that force-fed cooling can cool up to 925 W/cm^2 with heat transfer coefficient of $130,000 \text{ W/m}^2\text{K}$ using the nonaqueous refrigerant HFE-7100. These results demonstrated that FFMHX is a promising candidate for applications that require high heat flux cooling with high efficiency. Cetegen (2010) later proposed and tested a similar but improved test section by decreasing the measurement uncertainties and decreasing the two-phase flow instabilities. For two-phase FFMHX, three different heat sink designs incorporating microgrooved surfaces with microchannel widths between 21 and $60 \mu\text{m}$ were tested experimentally using refrigerant R-245fa, a dielectric fluid. It was demonstrated that FFMHX could cool a heat flux of 1.23 kW/cm^2 with a wall superheat of 56.2°C and pressure drop of 60.3 kPa.

A summary of this literature survey is given in Table 2.1. Two major conclusions can be drawn from this survey. First, FFMHX has the potential to achieve higher thermal performance values than TMHS. However, a comparison between the two needs a more systematic approach. One substantive method would be to compare the thermal performance of FFMHX with other conventional cooling technologies at optimum design and working conditions. Second, since all the parametric studies and optimization techniques used in previous studies are based on single-objective optimization methods, in order to obtain the real optimum

Table 2.1 Summary of related work on single-phase FFMHXs

Authors	Type of work	Microgrooved surface material (TSM) and working fluid (WF)	Microchannel hydraulic diameter (micron)	Reynolds number and flow regime	Parametrical study or optimization performed	Conclusion
Harpole and Enginger (1991)	2D analytical model	TSM: silicon WF: water	15–66	15–400 (laminar flow)	Yes	FFMHX could be used effectively for cooling high fluxes
Copeland (1995)	1D analytical model	TSM: low conductive material WF: water	8–64	(laminar flow)	Yes	There exist optimum points for microgrooved surface and manifold dimensions
Copeland and Behnia (1997)	3D numerical simulation using fluent	TSM: silicon WF: water	113–226	18–485 (laminar flow)	Yes	1D models based on straight channel flow cannot predict thermal performance of FFMHX
Kim and Chun (1998)	Experimental	TSM: copper WF: air	700–2000	(laminar flow)	Yes	FFMHXs can perform 30 % better compared with TMHS thermal performance
Ng and Poh (1999)	3D numerical simulation using ansys/flotran	TSM: silicon WF: water	113–226	10–800 (laminar flow)	Yes	1D models based on straight channel flow can under-predict thermal performance of FFMHX by 400 %
Ryu and Choi (2003)	3D numerical model	TSM: silicon WF: water	10–60	1–100 (laminar flow)	Yes	Compared with TMHS thermal performance, FFMHX can perform 50 % better with ten times better surface temperature uniformity
Jankowski and Everhart (2007)	Experimental	TSM: silicon and AlN WF: water	40–760	(laminar flow)	No	FFMHX needs to be optimized to achieve comparable better performance

(continued)

Table 2.1 (continued)

Authors	Type of work	Microgrooved surface material (TSM) and working fluid (WF)	Microchannel hydraulic diameter (micron)	Reynolds number and flow regime	Parametrical study or optimization performed	Conclusion
Xia and Liu (2008)	Experimental	TSM: silicon WF: aqueous surfactant solution	200	100–3500 (laminar and transitional flow)	No	Surfactants can decrease pressure drop at high temperatures and Reynolds numbers
Haller and Woias (2009)	Experimental and 3D numerical model	TSM: silicon WF: water	300–1200	10–3000 (laminar and transitional flow)	No	Creation of secondary flows at high <i>Re</i> numbers can enhance heat transfer

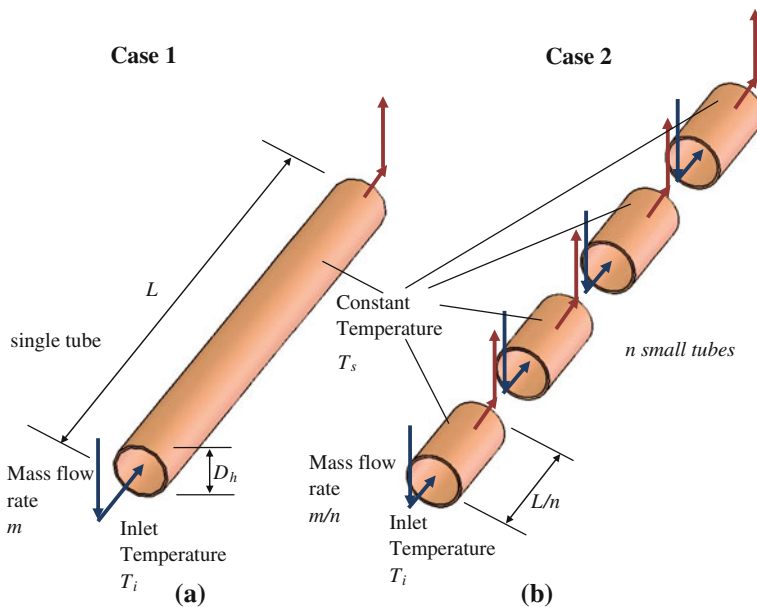


Fig. 2.3 Schematic of flow in **a** a single long channel and **b** multiple short channels (Cetegen 2010)

designs, a multiobjective optimization technique is necessary. With such a technique, the thermal performance could be optimized based on the most important objective functions, which in this case are heat transfer coefficient and pumping power. The objective should be to maximize the heat transfer coefficients while minimizing the pumping power.

2.2 Heat Transfer Analysis of FFMHX

Simple analyses can demonstrate the thermal performance advantages of FFMHX over traditional microchannel single-phase flow. Using heat transfer and pressure drop formulations for internal flow, the reduction in pumping power of the forced heat transfer (FFHT) flow configuration can be estimated. The procedure and assumptions used in this analysis are discussed in the following sections.

2.2.1 Heat Transfer and Pumping Power in Short Channels

Consider the two flow configurations shown in Figs. 2.3a, b. Case 1, shown in Fig. 2.3a, depicts flow in a single long tube with hydraulic diameter of D_h , tube

length L , mass flow rate \dot{m} , constant surface temperature T_s , and inlet temperature T_i . This case is analogous to a single channel in a TMHS with a highly conductive microgrooved surface base material. The second case, Case 2, shown in Fig. 2.3b, represents the same tube divided into n equal length, short tube segments. This case is analogous to an FFMHX flow configuration formed from a single microchannel. The mass flow rate running in each tube was divided equally, resulting in a mass flow rate of \dot{m}/n in each short tube. All other parameters, such as hydraulic diameter and inlet, outlet, and surface temperatures, were kept constant. At this stage, to further simplify the problem, the ratio of channel length to hydraulic diameter L/D_h for both cases was assumed to be high; therefore, entrance effects were neglected and flow was assumed to be fully developed. The flow in microchannels is generally laminar flow; therefore, the Reynolds number was assumed to be always below $Re < 2,300$. Also, the major pressure losses were assumed to be dominantly higher, and inlet and outlet minor losses were neglected. Heat was applied to the surface at constant temperature T_s .

It should be noted that in the following analysis, by assuming high L/D_h ratio, the developing regions in the short microchannels were neglected. This is a conservative approach since short microchannels in FFMHX can actually be optimized to utilize this heat transfer augmentation method, and efficiency can be improved dramatically. But the objective of the analysis in this chapter is to show the distinctive advantages of short channel systems over the traditional long channel ones, which will be proven even without including the developing region. With the addition of the developing heat transfer region, the discrepancy between the two systems would be even more pronounced.

Usually, the most important performance parameters considered in a heat sink design are overall heat transfer coefficient between the heated surface and coolant temperatures, and the pumping power. While the overall heat transfer coefficient is desired to be as high as possible to increase heat transfer efficiency, the pumping power values need to be minimized. Since these two parameters conflict, a reasonable comparison can be made by keeping one parameter constant and performing the comparison based on the other. Here, the overall heat transfer coefficients for Case 1 and Case 2 will be kept constant, and the pumping power will be evaluated.

It can be shown that with constant surface temperature assumption, the outlet fluid temperature $T_{o,1}$ for Case 1 can be calculated from (Incropera and DeWitt 2002) as:

$$\frac{T_s - T_{o,1}}{T_s - T_i} = \exp\left(-\frac{\pi D_h L \bar{h}}{\dot{m} c_p}\right) \quad (2.1)$$

where \bar{h} is the average heat transfer coefficient. For the current case, this value is constant along the tube and is equal to:

$$\bar{h} = h_z = Nu_T \frac{k}{D_h} = 3.66 \frac{k}{D_h} \quad (2.2)$$

Here $Nu_T = 3.66$ is the Nusselt number defined for fully developed flow in a tube with constant wall temperature (Incropera and DeWitt 2002), and k denotes the thermal conductivity of the working fluid. The heat transfer to the fluid is then calculated based on logarithmic mean temperature difference:

$$q_{\text{Case1}} = \bar{h}(\pi D_h L) \frac{(T_s - T_{o,1}) - (T_s - T_i)}{\ln \frac{T_s - T_{o,1}}{T_s - T_i}} \quad (2.3)$$

Similarly, for each short tube defined in Case 2 the outlet fluid temperature $T_{o,2}$ can be calculated as

$$\frac{T_s - T_{o,2}}{T_s - T_i} = \exp\left(-\frac{\pi D_h L / n}{\dot{m} / n c_p} \bar{h}\right) = \exp\left(-\frac{\pi D_h L}{\dot{m} c_p} \bar{h}\right) \quad (2.4)$$

The right-hand sides of Eqs. (2.1) and (2.4) are identical, which indicates that for the two cases the outlet temperatures are equal. The total heat transfer in Case 2 is then evaluated by substituting $T_{o,1} = T_{o,2}$ and summing the heat transfer surface as:

$$\begin{aligned} q_{\text{Case2}} &= \sum_{i=1}^n \bar{h}(\pi D_h L / n) \frac{(T_s - T_{o,2}) - (T_s - T_i)}{\ln \frac{T_s - T_{o,2}}{T_s - T_i}} \\ &= \bar{h}(\pi D_h L) \frac{(T_s - T_{o,1}) - (T_s - T_i)}{\ln \frac{T_s - T_{o,1}}{T_s - T_i}} \end{aligned} \quad (2.5)$$

Equations (2.3) and (2.5) are equal, which indicates that the heat transferred from both the single-tube configuration of Case 1 and the multiple tubes with the same hydraulic diameter and heat transfer area of Case 2 is the same. Since inlet temperature is constant and equal for both cases, the heat sink heat transfer coefficients will be the same as well.

The pumping power for a control volume is the product of volumetric flow rate and pressure drop:

$$P_{\text{pump}} = \Delta P \cdot \frac{\dot{m}}{\rho} \quad (2.6)$$

The major pressure losses for laminar flow in a tube can be calculated as:

$$\Delta P = f \frac{L}{D_h} \rho \frac{V^2}{2} \quad (2.7)$$

where $V = \frac{4\dot{m}}{\rho \pi D_h^2}$ is the mean fluid velocity in the tube and the pressure loss coefficient for fully developed laminar flow is defined as:

$$f = \frac{64}{Re} = \frac{64 \mu}{\rho V D_h} \quad (2.8)$$

Substituting Eqs. (2.7) and (2.8) into Eq. (2.6), the total pumping power required for Case 1 and Case 2 can be calculated as:

$$P_{\text{pump},1} = \left(\frac{128}{\pi} \frac{1}{D_h^4} \frac{\mu}{\rho^2} \right) L \dot{m}^2 \quad (2.9)$$

$$P_{\text{pump},2} = \sum_{i=1}^n \left(\frac{128}{\pi} \frac{1}{D_h^4} \frac{\mu}{\rho^2} \right) L/n(m/n)^2 \quad (2.10)$$

Based on these two equations the pumping power reduction can be calculated as:

$$\frac{P_{\text{pump},2}}{P_{\text{pump},1}} = \frac{1}{n^2} \quad (2.11)$$

Equation (2.11) demonstrates that for the same overall heat transfer coefficient, the split-flow configuration with multiple inlet and outlets has the potential to decrease the pumping power proportional to the square of the number of divisions. In other words, as long as the assumptions made above are valid, increasing the number of small channels by manifolding the flow always has a positive effect on decreasing the power consumption of the cooling system.

2.2.2 Heat Transfer and Pressure Drop for Thermally and Hydrodynamically Developing Flow

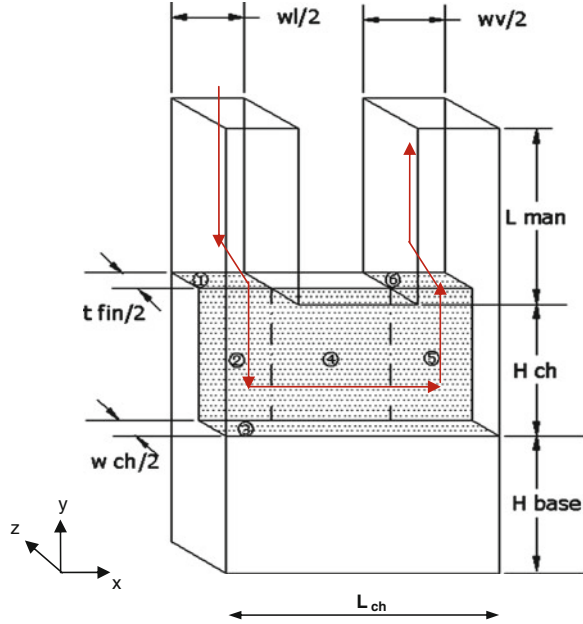
For the analysis performed in the previous section, it was assumed that the flow was fully developed along the whole tube. This assumption is not valid when the tube length over the tube hydraulic diameter ratio (L/D_h) is small. In this case, the heat transfer and momentum transfer occur mostly in the entrance region of the channel, where the hydrodynamic and thermal boundary layers are developing. Therefore, the heat transfer coefficient and friction factor in the entrance region depend on the distance from the entrance, Reynolds number, and fluid physical properties. These parameters may have a significant impact on thermal performance of FFMHX, where the heat transfer occurs mostly in the entrance region and the flow is hydrodynamically and thermally developing.

Assuming uniform velocity profile at the inlet, the hydrodynamic entry length $L_{\text{fd},h}$ for laminar flow in a tube is obtained from the following relation given by Langhaar (1942):

$$\left(\frac{L_{\text{fd},h}}{D} \right)_{\text{lam}} \approx 0.05 Re. \quad (2.12)$$

The friction factors in the hydrodynamically developing region are higher than those defined for fully developing flow. The skin friction and the additional momentum rate change due to change in the velocity profile are added together to

Fig. 2.4 Numerical computational domain (Cetegen 2010)



define the apparent friction coefficient. For circular tubes, Shah and London (1978) proposed the following correlation:

$$f_{app}Re = 344(x^+)^{-0.5} + \frac{\frac{1.25}{x^+} + (fRe)_{fd} - 344(x^+)^{-0.5}}{1 + 2.12 \times 10^{-4}(x^+)^{-0.2}} \quad (2.13)$$

where $(fRe)_{fd} = 64$ is defined for fully developed flow and x^+ is the nondimensional channel length defined as:

$$x^+ = \frac{L}{ReD} \quad (2.14)$$

For thermally developing laminar flows, Kays and Crawford (1980) proposed the following equation to calculate the thermal entry length $L_{fd,t}$:

$$\left(\frac{L_{fd,t}}{D}\right)_{lam} \approx 0.05RePr \quad (2.15)$$

For the combined hydrodynamically developing region and thermal entry region for laminar flow in a circular tube, the average Nusselt number is given by Sieder and Tate (1936):

$$\overline{Nu} = 1.86 \left(\frac{RePr}{L/D}\right)^{1/3} \left(\frac{\mu}{\mu_s}\right)^{0.14} \quad (2.16)$$

Equations (2.13) and (2.16) demonstrate that in the entry region, both heat transfer coefficients and pressure drop increase compared to fully developed flow. This result may have an important impact on thermal performance of FFMHX, where the length of the channels is usually comparable to hydraulic diameters. Given that pumping power and heat transfer coefficients are the most important heat sink design parameters, both hydrodynamic and thermal entry effects need to be considered. For water and liquid working fluids with Prandtl numbers greater than unity, the benefit of increased heat transfer is usually higher than the penalty from pressure drop.

2.3 Numerical Modeling of Single-Phase Heat Transfer in FFMHX

Building an exact analytical heat transfer model of a force-fed microchannel heat sink is not practical due to the geometry and flow complexities mentioned in previous sections. The most efficient and feasible way to analyze the heat transfer and flow in such heat sinks is to perform numerical simulations. To decrease computational time, however, several assumptions need to be made. For example, the numerical modeling of the real-scale complete heat sink shown in Fig. 2.1 using CFD tools is neither feasible nor practical and presents real challenges in terms of computational time. A practical solution for this problem is to define a computational domain consisting of a much smaller but repetitive part of the real-scale heat sink. A sample computational domain is shown in detail in Fig. 2.4. Due to the repetitive nature of the computational domain over the entire heat sink on the y - z and x - y planes, symmetric boundary conditions can be used at the boundary surfaces located at these planes. The model is a combination of the microgrooved surface modeled as solid material and the fluid that flows through the feed channels and the microchannels. Because the microgrooved surface is symmetrical, it is modeled as the base and half of a fin. The microchannel is modeled as half of a channel, and similarly the inlet and outlet feed channels are considered only half of the channel width.

The computational domain shown in Fig. 2.4 includes several assumptions:

- The flow rate in each feed channel is steady and equal. The inlet feed channels of an FFMHX have identical geometries, and they are fed from the same pressure source. The outlet feed channels are formed by the gap between two neighboring manifolds, and therefore the pressure loss for each unit cell is constant. The only exception is the feed channels at the edges (the first and last feed channels), where there is no counter-manifold to create symmetry.
- When using microgrooved surfaces fabricated by MDT, the fins and channels of the microgrooved surfaces are usually not straight and may have a slightly bent geometry, as shown in Fig. 2.4, and the fins may end with an unconventionally

Table 2.2 Boundary conditions applied to computational domain

Location of applied boundary condition	Boundary condition
$x = 0$	Symmetry
$x = L$	Symmetry
$z = 0$	Symmetry
$z = t_{\text{fin}}/2 + w_{\text{ch}}/2$	Symmetry
$y = 0$	Uniform heat flux of $q'' = 1 \text{ kW/cm}^2$
$y = H_{\text{base}} + H_{\text{ch}} + L_{\text{man}}$	Specified inlet mass flow rate
$0 < x < w_l/2$	
$0 < z < t_{\text{fin}}/2 + w_{\text{ch}}/2$	
$y = H_{\text{base}} + H_{\text{ch}} + L_{\text{man}}$	Pressure outlet (zero outlet static pressure)
$(L - w_l/2) < x < L$	
$0 < z < t_{\text{fin}}/2 + w_{\text{ch}}/2$	

sharp fin tip. Here, the microgrooved surface geometry can be simplified by assuming straight fin geometry with flat fin tips.

- The heat flux applied from the bottom of the microgrooved surface should be considered constant. Simulating a nonuniform heat flux distribution is not feasible, since any variation in the X and Z directions will violate the symmetry conditions.
- The thermal properties (thermal conductivity) of the metal substrate are isotropic. Similarly, the symmetry boundary condition can be applied only for solids with isotropic thermal properties in the X and Z directions.
- The heat transfer through the manifolds is neglected, and the manifolds are considered adiabatic. There are two means of possible heat transfer in the manifolds. The first mechanism is the heat transfer through the incoming and outgoing fluid streams in the neighboring inlet and outlet feed channels. Here, a temperature gradient forms due to the temperature difference in the fluid streams, where fluid leaving the heat sink is hotter than the inlet steam due to the energy gained during heat transfer on the microgrooved surface. The heat transfer caused by this temperature gradient can be neglected by assuming that manifolds are made of poor conductive material such as low conductivity plastic. The second possible heat transfer mechanism is the thermal conduction through the tip of the fins to the manifold. In many practical applications, the manifolds are not bonded to the microgrooved surface, but rather kept in place by compressive forces. This configuration allows the microgrooved surfaces to be cleaned by easily disassembling the heat sinks in case of fouling and microchannel clogging. As shown in Fig. 2.4, the fin tips usually have a sharp edge, which creates a line of contact when compressed with the manifold top face, thereby creating a relatively high thermal contact resistance. To further simplify the problem and eliminate uncertainties associated with linear thermal contact resistance, an adiabatic manifold should be assumed for the numerical simulations.

2.3.1 Numerical Simulation of a Sample FFMHX

As an example, a typical FFMHX was numerically simulated and analyzed. The purpose of these numerical simulations was to demonstrate the working principle and to provide an initial design concept. The selected sample FFMHX configuration consisted of a microgrooved surface with channel height of $H_{\text{ch}} = 480 \mu\text{m}$, fin thickness of $t_{\text{fin}} = 48 \mu\text{m}$, microchannel width of $w_{\text{ch}} = 72 \mu\text{m}$, and base thickness of $H_{\text{base}} = 400 \mu\text{m}$, and manifold system with inlet feed channel width of $w_l = 400 \mu\text{m}$, outlet feed channel width of $w_v = 400 \mu\text{m}$, and total channel length of $L_{\text{man}} = 2 \text{ mm}$. The microgrooved surface material and working fluid were copper and water, respectively.

2.3.1.1 Boundary Conditions and Numerical Domain

A complete list of applied boundary conditions is given in Table 2.2, based on the coordinate system shown in Fig. 2.4. Boundaries not included in the table were selected as adiabatic wall as default. The specified boundary condition for the inlet mass flow rate uses flow rate as input and calculates the static pressure based on the flow field. Therefore, the inlet static pressure is not known as *a priori* until the convergence is obtained. Similarly, the outlet boundary condition is specified as static pressure, and the total pressure is calculated after convergence is obtained.

The analyses were based on two output functions, the heat transfer coefficient and pumping power. Once the numerical convergence was achieved, these functions were evaluated based on post-processing data obtained from the flow field. The overall heat transfer coefficient was defined for the temperature difference between average surface temperature and inlet fluid temperature:

$$h = \frac{q^n}{\bar{T}_{\text{surf}} - \bar{T}_{\text{in}}} \quad (2.17)$$

where the temperature values were area averaged over the surface as:

$$\bar{T} = \frac{1}{A} \int T \cdot dA \quad (2.18)$$

The pumping power was calculated for the unit base area. Pumping power has been defined by many researchers (Choo and Kim 2010b, c; Choo et al. 2012) as the product of total pressure difference between inlet and outlet boundaries and volumetric flow rate passing through the unit base area heat sink:

$$P'_{\text{pump}} = \frac{\dot{m}(\bar{P}_o - \bar{P}_i)}{\rho \left[L \left(\frac{l_{\text{fin}}}{2} + \frac{w_{\text{ch}}}{2} \right) \right]} \quad (2.19)$$

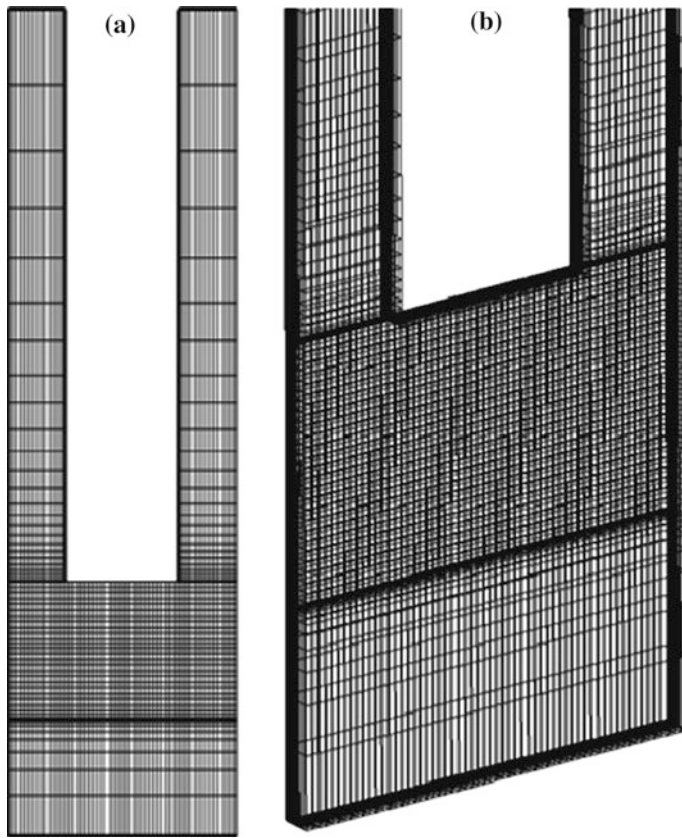


Fig. 2.5 **a** Front view and **b** perspective view for grid generated for $H_{ch} = 480 \mu\text{m}$, $w_{ch}/2 = 36 \mu\text{m}$, $t_{fin}/2 = 24 \mu\text{m}$, $L = 800 \mu\text{m}$, $w_f/2 = 200 \mu\text{m}$, $w_v/2 = 200 \mu\text{m}$, $L_{man} = 2 \text{ mm}$, $H_{base} = 400 \mu\text{m}$ (Cetegen 2010)

where the pressure values are also area averaged at inlet and outlet:

$$\bar{P} = \frac{1}{A} \int P \cdot dA \quad (2.20)$$

The pumping power definition in Eq. (2.19) is practical for the extrapolation of pumping power for heat sinks with different base areas. In this case, for constant microchannel mass flux and microgrooved surface geometry, the pressure difference for the heat sink will remain the same, while the flow rate will increase linearly by increasing the heat sink base area.

Since heat transfer and pumping power are functions of flow rate, the flow conditions need to be defined. This is accomplished by introducing the Reynolds number based on flow in the straight channel part of the microchannel defined as:

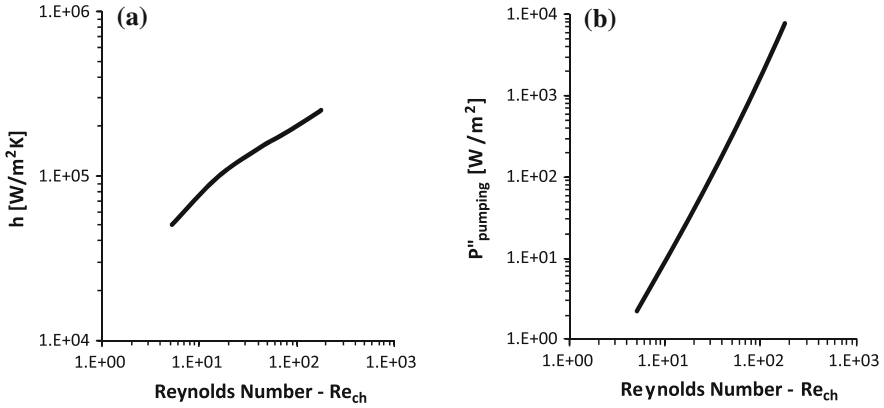


Fig. 2.6 **a** Variation of effective heat transfer coefficient with Reynolds number; **b** variation of pumping power with Reynolds number (Cetegen 2010)

Table 2.3 Numerical simulation results

	Unit	Case #1	Case #2	Case #3
Re	(-)	5	43	177
h	(W/m ² K)	50,022	150,035	25,0094
P''_{pump}	(W/m ²)	2.2	227.3	7888.8

$$Re = \frac{V_{ch} D_h}{\nu} \quad (2.21)$$

where

$$V_{ch} = \frac{\dot{m}}{\rho H_{ch} w_{ch}} \quad (2.22)$$

and

$$D_h = \frac{4H_{ch} w_{ch}}{2(H_{ch} + w_{ch})} \quad (2.23)$$

Here, \dot{m} is the total mass flow rate, V_{ch} is the average velocity and D_h is the hydraulic diameter, all defined for the flow in the straight part of the microchannel. All other geometrical dimensions are shown in Fig. 2.4.

The resulting computational grid is shown in Fig. 2.5. A grid independency study was performed by selecting a base case and refining mesh to generate five different grids, each consisting of 35,840, 48,576, 68,850, 98,604, and 137,280 cells. The heat transfer coefficient and pumping power per unit heat sink area were used as parameters for checking the grid independency. The results indicate that the case with 68,850 cells is reasonably accurate for the current study. When the

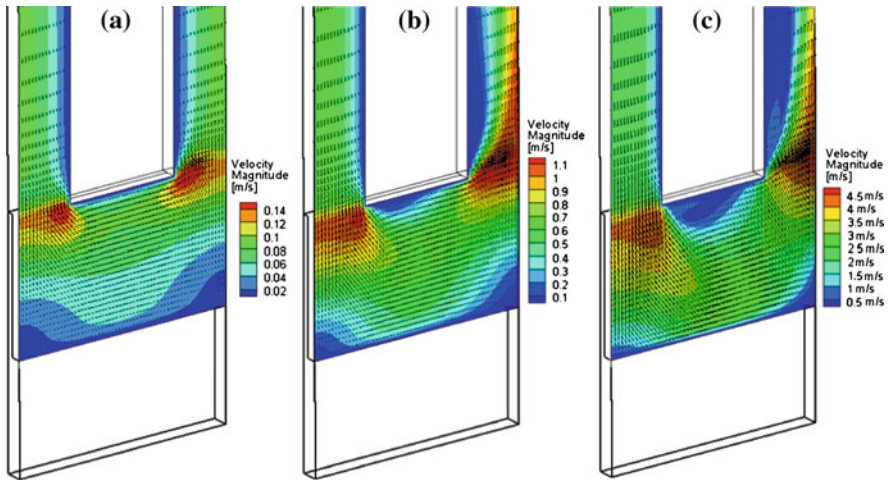


Fig. 2.7 Velocity vectors and velocity magnitude distribution at $z = 0$ for **a** Case #1 at $h = 50,000 \text{ W/m}^2\text{K}$; **b** Case #2 at $h = 150,000 \text{ W/m}^2\text{K}$; **c** Case #3 at $h = 250,000 \text{ W/m}^2\text{K}$ (Cetegen 2010)

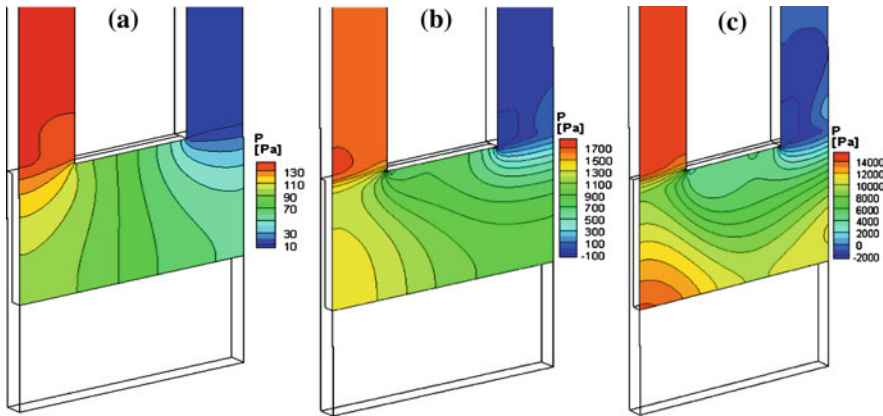


Fig. 2.8 Static pressure distribution at $z = 0$ for **a** Case #1 at $h = 50,000 \text{ W/m}^2\text{K}$; **b** Case #2 at $h = 150,000 \text{ W/m}^2\text{K}$; **c** Case #3 at $h = 250,000 \text{ W/m}^2\text{K}$ (Cetegen 2010)

number of cells was increased by almost two times, the variations in heat transfer coefficient and pumping power were calculated to be 0.29 and 0.47 %, respectively.

For all calculated cases, the convergence factor for continuity, three momentum equations, and energy equations were set as $1\text{e-}5$, $1\text{e-}5$, and $1\text{e-}11$. The computational run time was 25 min on a PC with an Intel Pentium D 3.4 Ghz processor and 2 GB of memory.

2.3.1.2 Numerical Results

The numerical simulations covered heat transfer coefficients ranging from 50,000 to 250,000 W/m²K. The resulting variations of overall heat transfer coefficient and pumping power with Reynolds number are given in Fig. 2.6a and b plotted on log–log charts. For these plots, the results indicate an almost linear variation for both heat transfer coefficients and pumping power values with increased flow rate. Having a slope different than one, the linear trend on a log–log plot indicates a power-law dependence. For fully developed laminar flow in a straight microchannel with constant cross-section area, the pumping power is proportional to the square of the channel velocity or Reynolds number, indicating a power-law trend with power coefficient of two. On the other hand, the pumping power curve obtained in Fig. 2.6b has a power-law coefficient of ≈ 2.4 . This in turn may suggest the influence of strong developing flow, secondary flows or other recirculation zones not present in straight microchannel flow.

To analyze the possible effects of these parameters, three different specific cases resulting in heat transfer coefficients of 50,000, 150,000, and 250,000 W/m²K were selected as main case studies. The three cases are labeled Case #1, Case #2, and Case #3 and represent the low, medium, and high heat transfer coefficient designs. For each case, the mass flow rate was adjusted to give the targeted h value. The resulting numerical values of heat transfer coefficient and pumping power for these cases are given in Table 2.3.

The velocity vectors and velocity magnitude distribution on the mid-symmetry plane of $z = 0$ are shown in Fig. 2.7a, b and c for three case studies at $h = 50,000$, 150,000, and 250,000 W/m²K, respectively. The flow trend observed in the three cases is explained as follows. The fluid enters the system through the inlet feed channel located on the left. It becomes fully developed and then reaches the microgrooved surface, where it contracts as it is forced into the microchannel. The area contraction creates a local decrease in static pressure and a local maximum in velocity magnitude. Due to entrance effects, the flow is hydrodynamically and thermally developing, starting with the inlet into the microchannel. The flow then turns 90° to the right as it undergoes an area expansion due to the higher flow area of the microchannel compared to the inlet flow area. The velocity magnitude distribution in this straight part of the microchannel is stratified in the y direction and with little variation in the x direction. The fluid exits the microchannel by making a second 90° turn and expanding into the outlet feed channel. A second velocity maximum is present just before the exit from the microchannel due to the flow area contraction–expansion effect.

While the results of the three cases shown in Fig. 2.7 have several common flow characteristics as discussed above, they differ in the physical mechanisms that characterize the flow. For example, at low Reynolds number flows (Fig. 2.7a), the inertial forces of the fluid entering the microchannel are comparable to the viscous forces in the microchannel. Therefore, the inertial forces of the incoming fluid are insufficient to push the fluid to the bottom of the microchannel and to create an impingement zone. Instead, due to the significant effect of viscous forces, the fluid

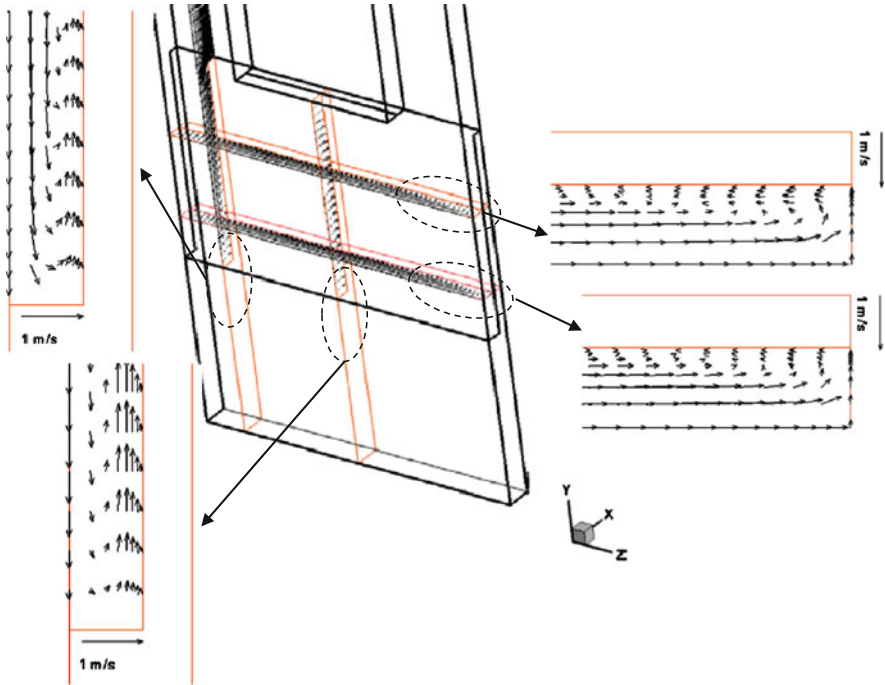


Fig. 2.9 Velocity vectors created by secondary flows at several cross-sections in the computational domain for Case #3 at $h = 250,000 \text{ W/m}^2\text{K}$ and $De = 61$ (Cetegen 2010)

follows the path with the least friction losses, which creates a bypass zone just under the manifold between the inlet and outlet feed channels. The bypass zone in turn creates stratification in velocity distribution in the y direction with high velocities accumulated on the top and low velocity flow close to the bottom of the microchannel. The flow maldistribution is even more pronounced in the bottom microchannel regions under the inlet and outlet manifolds with the creation of “dead zones” with velocities below 0.02 m/s . This effect can be also explained by studying the static pressure distribution along the microchannel, as given in Fig. 2.8a for low Reynolds number flows. The static pressure distribution is uniform, and starting from the microchannel inlet, it decreases gradually along the microchannel length until it reaches the outlet zone. Due to the fluid bypass effect present at the top region, the fluid is not impinging the channel bottom, and no pressure increase is observed in this region.

Increasing the Reynolds number, by increasing the flow rate (Figs. 2.7b, c), leads to a different flow trend. First of all, the inertial force of the fluid entering the microchannel is high enough to push the liquid to the bottom of the microchannel and to create an impingement zone. The fluid first decelerates as it approaches this stagnation zone, turns the 90° bend, and then starts to accelerate again as it moves toward the straight part of the microchannel. The static pressure in the

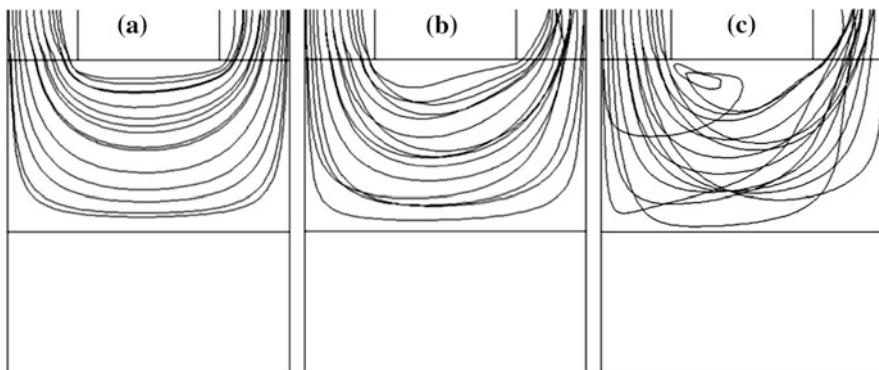


Fig. 2.10 Pathlines at $z = 0$ plane for **a** Case #1 at $h = 50,000 \text{ W/m}^2\text{K}$ and $De = 2$; **b** Case #2 at $h = 150,000 \text{ W/m}^2\text{K}$ and $De = 16$; **c** Case #3 at $h = 250,000 \text{ W/m}^2\text{K}$ and $De = 61$ (Cetegen 2010)

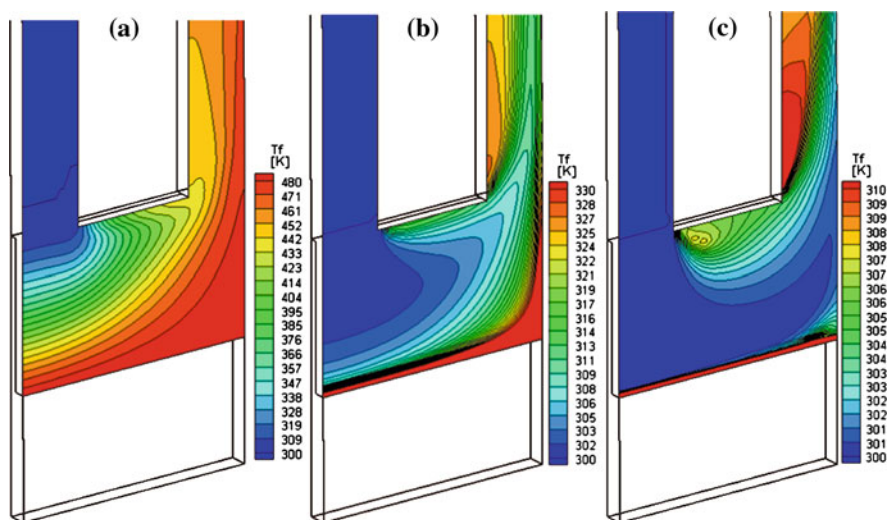


Fig. 2.11 Working fluid temperature distribution at $z = 0$ for **a** Case #1 at $h = 50,000 \text{ W/m}^2\text{K}$; **b** Case #2 at $h = 150,000 \text{ W/m}^2\text{K}$; **c** Case #3 at $h = 250,000 \text{ W/m}^2\text{K}$ (Cetegen 2010)

impingement zone increases due to momentum exchange of this turning fluid (Figs. 2.8b, c). Second, the high inlet velocities and sharp corners of the manifold lead to flow separation that creates a recirculation zone under the manifold. The recirculation zone grows by increasing the Reynolds number. Interestingly, the velocity stratification for this case is opposite the low Reynolds number case. There is a high velocity core close to the bottom of the microchannel and low velocity recirculation zone at the top of the microchannel. A second recirculation zone is present at the bottom of the microchannel zone, under the outlet feed

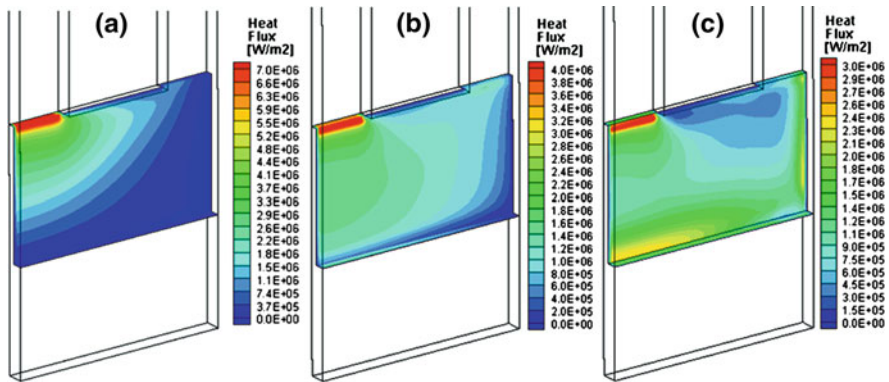


Fig. 2.12 Fin feat flux distribution for **a** Case #1 at $h = 50,000 \text{ W/m}^2\text{K}$; **b** Case #2 at $h = 150,000 \text{ W/m}^2\text{K}$; **c** Case #3 at $h = 250,000 \text{ W/m}^2\text{K}$ (Cetegen 2010)

channel. In this region, the flow turns toward the outlet of the microchannel and does not flow deeply into the corner of the channel, which has much higher flow resistance. The third recirculation zone appears just after the outlet from the microchannel, in the outlet feed channel. Similarly, the velocity distribution tends to be stratified, with the high velocity core close to the center of the outlet feed channel. This separation is the result of the high outlet velocities at the sharp manifold corner.

In addition to the flow conditions discussed above, the flow velocity can affect the flow field by creating secondary flows. Due to the bulk flow rotation, a centrifugal force acting from the center of rotation to the channel bottom becomes present, and the fluid at the side walls is pressed in the opposite direction. This, in turn, forces the fluid to generate vortex pairs that can fill the channel cross-section. The magnitude of the centrifugal force depends on the flow velocity and radius of curvature of the bend and is a function of the Dean number. The development of secondary flows changes both heat transfer and flow characteristics. The vortices create continuous fluid mixing by moving the colder fluid at the center to the side walls of the microchannel, thus enhancing the convective heat transfer. This process disturbs and reduces the thickness of the thermal boundary layer that develops at the inlet to the microchannel. On the pressure drop side, however, due to the additional flow energy associated with vortices, the pumping power required to drive the fluid in a curved pipe will be always higher than straight tube and channel geometries at the same flow rate. These conflicting objectives of heat transfer efficiency and pumping power need to be considered to clearly evaluate the possible benefits of secondary flows.

Velocity vectors at several cross-sections in the computational domain for Case #3 are shown in Fig. 2.9. As the fluid starts to turn at both the first and second bends, vortex pairs are created in the microchannel as the fluid in the center is pushed down and forces the liquid close to the walls to move in the opposite direction. Due to symmetry conditions, only one half of the channel,

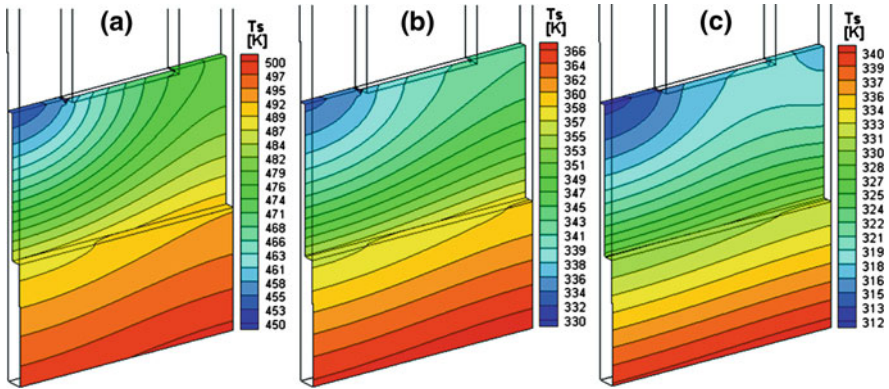


Fig. 2.13 Temperature contours of fin surface, microchannel bottom wall and base material for **a** Case #1 at $h = 50,000 \text{ W/m}^2\text{K}$; **b** Case #2 at $h = 150,000 \text{ W/m}^2\text{K}$; **c** Case #3 at $h = 250,000 \text{ W/m}^2\text{K}$ (Cetegen 2010)

and therefore only one vortex, is shown in the figure. The pathlines and transition between flow regimes at different Reynolds number flows are shown in Fig. 2.10a, b and c. The pathlines are uniform and almost symmetric, with no disturbance in the flow. As the Reynolds number is increased in Case #2 and later in Case #3, the centrifugal forces start to become important. The vortices formed during flow turning disturb the flow, and the pathlines show a less uniform pattern. As seen in Fig. 2.10c, due to secondary flows and the mixing effect, the pathlines can cross over each other on the plane of view.

The fluid temperature distribution at the symmetry plane of $z = 0$ is shown in Fig. 2.11a, b and c for Case #1, Case #2 and Case #3, respectively. Two different trends become important as the flow Reynolds number goes from low to high. First, the temperature rise of the fluid is significant at low flow rates. This is expected, since the mass flux is lower and the fluid can be heated much more before exiting the microchannel. Second, the velocity stratification shown in Fig. 2.7 also creates temperature stratification. The low velocity zones close to the bottom of the microchannel at low Reynolds number flows and “dead zones” in the high Reynolds number cases create high temperature zones. Similarly, the relatively low velocities allow the liquid to be heated for longer times, and therefore a temperature difference is observed in these regions.

The heat flux distribution on the fin and microchannel base for the three cases is shown in Fig. 2.12a, b and c. Although the mass flux has a significant effect on heat flux distribution on the fin surface, the maximum heat flux always occurs at the inlet region to the microchannel. This global maximum is the result of the large temperature difference between the fluid and surface and the significant entrance region effects where the thermal boundary layer is relatively thin and heat transfer resistance is low.

At low Reynolds number flows (Fig. 2.12a) the heat transfer efficiency decreases due to increase in noneffective areas that do not contribute to heat

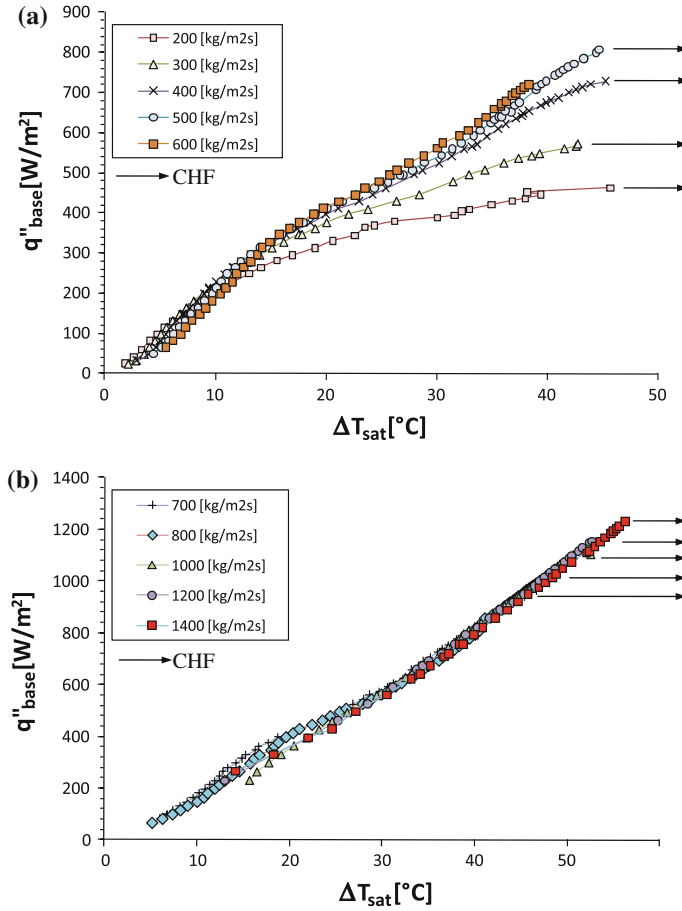


Fig. 2.14 Boiling curves for R-245fa at **a** $200 < G < 600$ kg/m²s and **b** $700 < G < 1400$ kg/m²s (Cetegen 2010)

transfer. The temperature difference between the bulk liquid and surface is low in these regions. The heat transfer characteristic changes significantly with higher Reynolds number flows (Fig. 2.12c). First, the heat flux becomes more uniformly distributed along the fin surface with the heat flux gradient decreasing slightly along the microchannel length. However, local minimums are present at the heat transfer surfaces under the recirculation zones. The fluid trapped in the recirculation zones has high bulk temperatures, which decrease the convective heat transfer efficiency. Second, the secondary local maxima starts to appear close to the impingement zones under the inlet and outlet feed channels. Similar local high heat transfer zones were reported by Copeland (1995), Copeland et al. (1997) and Ng and Poh (1999). Close to the impingement zones, the local fluid acceleration and vortices created during the flow turning have the effect of reducing the thermal

boundary layer thickness and enhancing heat transfer. It should be noted that these local high heat transfer zones are a strong function of Reynolds and Dean numbers.

Finally, the surface temperature distributions on the fin surface, microchannel base, and middle of the base material are shown in Fig. 2.13a, b and c for the selected three reference cases. The minimum fin temperature occurs close to the tip of the fin region, where the fluid enters the microchannel. Due to high heat transfer coefficients and relatively large temperature differences between the surface and fluid, the local fin temperature can decrease significantly. At low Reynolds number flows, all the heat transferred to the fluid is localized at the inlet region with heat flowing from all directions, perpendicular to the isotherms shown in Fig. 2.13a. Increasing the flow rate to higher Reynolds numbers (Fig. 2.13a and b) increases the heat transfer efficiency and significantly decreases the heat sink temperatures. On the other hand, the temperature isotherms become more horizontal, indicating a more uniform heat flow from the bottom of the base material to the fin heat transfer surface.

2.4 Two-Phase Heat Transfer in FFMHX

The FFHT flow configuration can be very beneficial for two-phase heat transfer applications. First, as discussed in single-phase flow, the overall system pressure drop decreases dramatically. This is a key advantage of FFMHX over traditional cooling technologies such as microchannel heat sinks, where the cooling capacity is mainly dictated by the pressure drop limitations. When working in two-phase heat transfer mode, large pressure differences between the inlet and outlet of the heat sink create significantly high saturation temperature differences. This, in turn, creates an unwanted temperature gradient along the flow and eliminates the isothermal flow conditions. Second, as the system pressure drop is lowered, the system pumping power is also decreased. This is also a key parameter for systems running continuously for long periods of time. Third, as the microchannel lengths become shorter and shorter, two-phase flow tends to become more stable. For example, for the same flow rate and outlet qualities, a shorter tube can experience much higher critical heat flux values when compared with a longer one. Also, when the microchannel length is comparable with its hydraulic diameter, the bubble dynamics observed in microchannels are believed to become more stable. Here, the fast growing bubble can reach the channel outlet faster than it can in traditional long microchannels.

Cetegen (2010) experimentally investigated force-fed flow boiling using copper microgrooved surfaces and a refrigerant, R-245fa, as the working fluid. The fins of the microgrooved surface were 480 μm high and 85 μm wide, while the microchannel gap was 42 μm . The experimental tests were performed at 10 different mass flux conditions ranging from 200 to 1,400 $\text{kg/m}^2\text{s}$, as shown in Fig. 2.14a and b. The boiling curves are plotted for the base heat flux q''_{base} versus wall superheat ΔT_{sat} , which is the temperature difference between

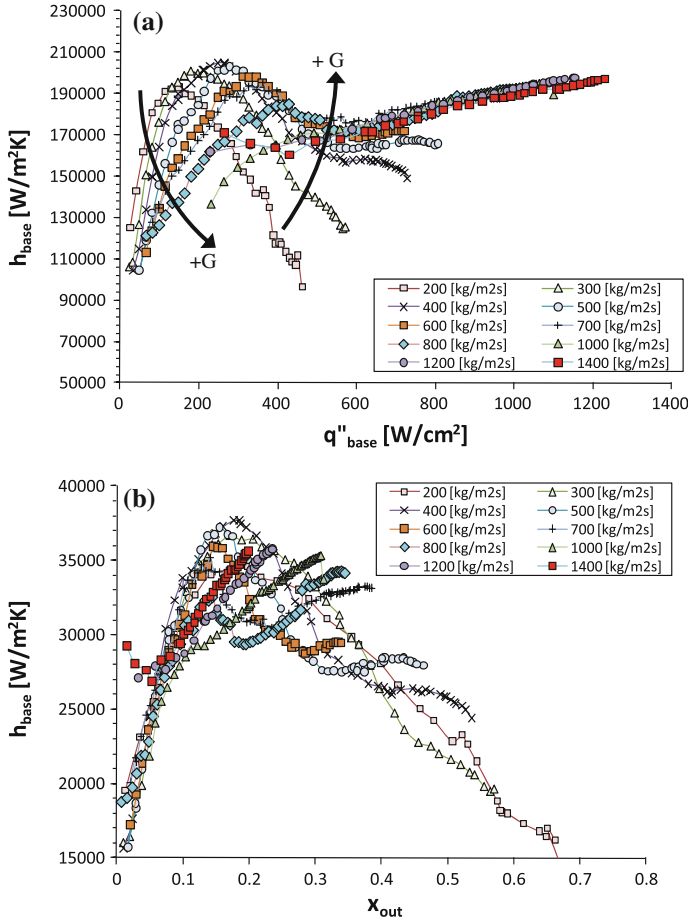


Fig. 2.15 **a** Heat transfer coefficient based on base area versus base heat flux and **b** heat transfer coefficient based on wetted area versus outlet quality for refrigerant R-245fa (Cetegen 2010)

average base surface temperature and average saturation temperature. The trend of the curves can be summarized as follows. For low to medium heat fluxes of $q''_{\text{base}} < 300 \text{ W/cm}^2$, the boiling curves show an almost linearly increasing trend with slightly different slopes. In this region, the wall superheat increases when going to higher mass fluxes at a constant heat flux. This implies higher heat transfer efficiency at lower mass fluxes. On the other hand, when heat fluxes increase above $q''_{\text{base}} > 300 \text{ W/cm}^2$, the trend is reversed, and departures from the main trend are observed for low to medium mass fluxes of $200 < G < 600 \text{ kg/m}^2\text{s}$. The departing curves have a smaller slope on the chart, which indicates less heat transfer for a given wall superheat; therefore, the heat transfer efficiency is expected to decrease compared with the main trend. The slope will continue to decrease until it reaches CHF conditions.

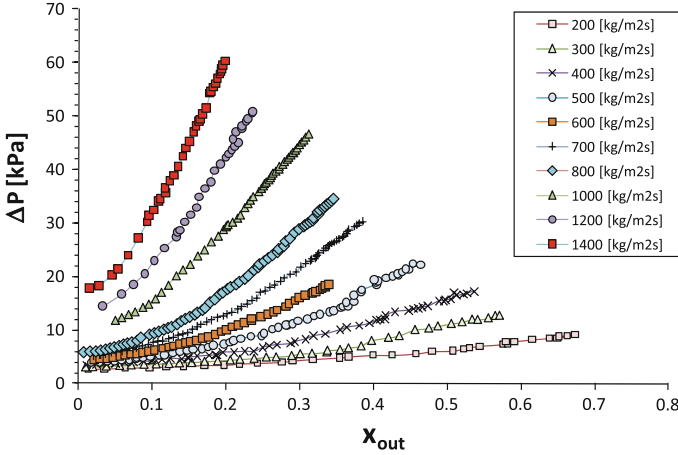


Fig. 2.16 Pressure drop values versus outlet quality for refrigerant R-245fa (Cetegen 2010)

The heat flux values where the CHF was obtained are shown with the black arrow, denoting a large temperature jump for a small increase in heat flux.

For medium to high mass fluxes and heat fluxes of $G > 600 \text{ kg/m}^2\text{s}$ and $q''_{\text{base}} > 600 \text{ W/cm}^2$, the boiling curves increase in a linear fashion and almost overlap. In contrast to the low mass flux cases, the CHF condition here is achieved along the straight overlapping part of the boiling curve and does not show early performance degradation. The maximum achievable heat flux was $q''_{\text{base}} = 1.23 \text{ kW/cm}^2$, corresponding to a wall superheat of $\Delta T_{\text{sat}} = 56.2^\circ\text{C}$.

For the same set of data, the heat transfer coefficients based on heat sink base area versus base heat flux variation are given in Fig. 2.15a. This classification is more convenient for heat sink designers since the definitions are based on the targeted cooling area and are not dependent on enhanced area parameters such as channel aspect ratio or fin efficiency. Figure 2.15b shows the heat transfer coefficients based on wet channel area versus outlet quality. This definition is useful for comparing the hydraulic and thermal performances of different microchannel geometries of microgrooved surfaces. It is important to note that these two graphs are not independent because for a fixed heat flux and mass flux there exists only one outlet quality. In other words, for a constant mass flux case, to change the outlet equilibrium quality the heat flux needs to be changed and vice versa.

As shown in Fig. 2.15a, at mass fluxes below $G < 500 \text{ kg/m}^2\text{s}$ the heat transfer coefficient curves show a bell-like curve starting with an initially increasing trend and then decreasing gradually until the CHF occurs. Here, the increase in heat transfer coefficients for all mass fluxes has a similar slope, while the decreasing trend is more dependent on mass flux. The increase in mass flux decreases the slope of the decreasing part of the curve, indicating an improvement in heat transfer and less severe performance degradation. The maximum peak point remains between $190,000 < h_{\text{base}} < 200,000 \text{ W/m}^2\text{K}$ and shifts toward higher

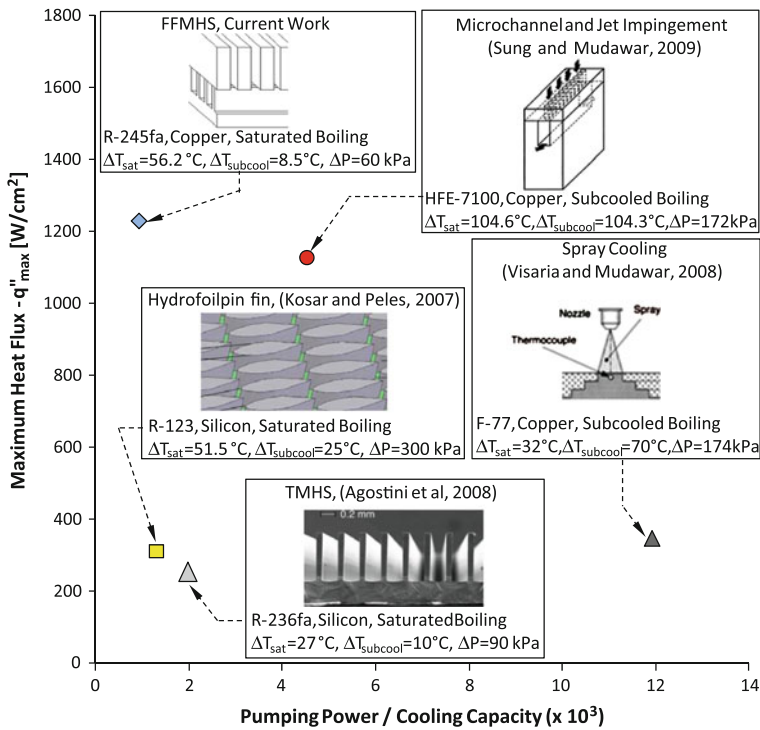


Fig. 2.17 Thermal performance comparison of different high heat flux cooling technologies (Cetegen 2010)

heat fluxes with increasing mass flux. It is interesting to note from Fig. 2.6b that the maximum heat transfer coefficients at these flow rates remain almost constant at $x_{out} \approx 0.15$. Here, the steep increasing trend of heat transfer coefficients may suggest a flow regime dominated mostly by nucleate boiling, which is a function of surface heat flux. The decreasing trend observed after the maximum may be the result of local dryouts, which become less severe as the mass flux increases.

For heat transfer coefficients obtained for higher mass fluxes of $G > 500 \text{ kg/m}^2\text{s}$, the trend shifts, as seen in Fig. 2.15a. As the mass flux increases, the peak previously seen at lower mass fluxes further decreases and diminishes after $G = 1,000 \text{ kg/m}^2\text{s}$. At the same time, the previously decreasing trend is also eliminated, and for high mass fluxes, both effects create a slow but monotonically increasing trend. More interestingly, all curves collapse altogether, forming a single line on the graph. This trend may suggest a convective boiling-dominated heat transfer regime, since the heat transfer coefficients are slightly dependent on heat flux but are more dependent on outlet quality and mass flux (Fig. 2.15b). Another observation from these graphs is the trend of heat transfer coefficient before reaching CHF. For low mass fluxes and the bell-like curve trend, the CHF always occurs when the heat transfer coefficients have a decreasing trend. On the other hand, at high mass fluxes, the boiling crisis

phenomenon occurs on the curve shown in Fig. 2.15a, where all the heat transfer coefficients overlap and have a slightly increasing trend.

The pressure drop variation versus outlet equilibrium quality is shown in Fig. 2.16. As expected, the pressure drop of the FFMHX is a function of both mass flux and outlet quality. For a constant mass flux, the pressure drop values show an exponential-like increase at low outlet quality values and a linear trend at higher outlet qualities. At the lowest tested mass flux of $G = 200 \text{ kg/m}^2\text{s}$, the system pressure drop is less than 10 kPa, corresponding to a saturation temperature change of less than 1.5°C . On the other hand, when the system works at high mass fluxes the saturation temperature change can be significant and should be carefully considered in the design stages. A very large saturation temperature difference can increase the surface temperature non-uniformity of the heat sink base. For example, for $G = 1,400 \text{ kg/m}^2\text{s}$ the maximum pressure drop was 60.4 kPa, which corresponds to a saturation temperature variation of 7.8°C .

2.4.1 Performance Comparison of FFMHX with Other High Heat Flux Cooling Technologies

As mentioned in the previous section, the highest critical heat flux obtained for force-fed two-phase heat transfer was $q'' = 1230 \text{ W/cm}^2$ measured for average wall superheat of 56.2°C and subcooling of 8.5°C . The corresponding pressure drop was measured as 60.3 kPa, and pumping power was calculated as 1.13 W. The heat sink footprint area was $7.8 \times 7.8 \text{ mm}^2$. As a general design rule, a heat sink should perform at high heat fluxes with low wall superheat, low subcooling, low pressure drop, and low pumping power. Therefore, compared to single-phase heat transfer, it is more challenging to compare cooling technologies for two-phase heat transfer mode because the heat sink performance is dependent on many more parameters. Nevertheless, a quantitative comparison can still be made by plotting the data over the two most important parameters. For this purpose, the two comparison parameters were selected as maximum heat flux and pumping power over cooling capacity ratio. For these parameters, the performance of FFHT was compared with other competing high heat flux cooling technologies (Sung and Mudawar 2009; Visaria and Mudawar 2008; Kosar and Peles 2007; Agostini et al. 2008), and the resulting graph is shown in Fig. 2.17. It should be noted, however, that the comparison parameters were selected based on their importance to the objective of the study. For example, for a comparison based on heat transfer efficiency of the y axis can be replaced with heat transfer coefficient h .

The technology comparison shown in Fig. 2.17 clearly indicates that the FFMHX technology can remove much higher heat fluxes (much higher heat transfer coefficients) with substantially less pumping power requirements than any of the applicable cooling technologies investigated. More importantly, this is

accomplished with a reasonable wall superheat, with low or little subcooling and moderate pressure drops. Another important point for the comparison chart is that no two-phase optimization was reported for any of the heat sink designs. For optimum conditions, the sequence and location of points on the graph may be significantly different. Therefore, future comparisons of the technologies should consider the effect of optimum design on thermal performance.

Next Generation Microchannel Heat Exchangers

Ohadi, M.M.; Choo, K.; Dessiatoun, S.; Cetegen, E.

2013, XII, 116 p. 101 illus., 13 illus. in color., Softcover

ISBN: 978-1-4614-0778-2